INTERNATIONAL JOURNAL FOR NUMERICAL METHODS IN FLUIDS
Int. J. Numer. Meth. Fluids 2003; **42**:323–348 (DOI: 10.1002/fld.524)

Spectral element method for viscoelastic flows in a planar contraction channel

Sha Meng[1], Xin Kai Li[1,2,*,†] and Gwynne Evans[2]

[1]*Shenyang Institute of Automation, Chinese Academy of Science, Shenyan, China*
[2]*Institute of Simulation Sciences, Faculty of Computing Science and Engineering, De Montfort University, Leicester LE1 9BH, England, U.K.*

SUMMARY

A new algorithm, which combines the spectral element method with elastic viscous splitting stress (EVSS) method, has been developed for viscoelastic fluid flows in a planar contraction channel. The system of spectral element approximations to the velocity, pressure, extra stress and the rate of deformation variables is solved by a preconditioned conjugate gradient method based on the Uzawa iteration procedure. The numerical approach is implemented on a planar four-to-one contraction channel for a fluid governed by an Oldroyd-B constitutive equation. The behaviour of the Oldroyd-B fluids in the contraction channel is investigated with various Weissenberg numbers. It is shown that numerical solutions obtained here agree well with experimental measurements and other numerical predictions. Copyright © 2003 John Wiley & Sons, Ltd.

KEY WORDS: spectral element method; viscoelastic flow; planar contraction channel; an Oldroyd-B fluid

1. INTRODUCTION

Despite much progress in the prediction of fluid flow, viscoelastic flow is an example of a field in which numerical techniques are still generally inadequate to describe flows in regimes of technological importance. This inadequacy is particularly acute when one considers flows with large stress gradients for time-dependent fluids. A geometrical singularity, such as a discontinuous boundary point or a boundary with discontinuous boundary conditions, is a principle source of steep gradients. The aim of this study is to provide insight into the numerical behaviour associated with a spectral element approach simulating viscoelastic complex fluids with differential equations as the base of the model rather than the alternative base such as an integral formulation.

* Correspondence to: Xin Kai Li, Institute of Simulation Science, Faculty of Computing Science and Engineering, Hawthom Building, De Montfort University, Leicester LE1 9BH, U.K.
† E-mail: xkl@dmu.ac.uk

Received November 2001
Revised 18 November 2002

Viscoelastic fluids are polymeric materials in which the state of stress depends on the history of the deformation, in contrast to a Newtonian fluids in which the stress depends only on the instantaneous rate of deformation. Viscoelastic fluids may exhibit behaviour that differs significantly from that of Newtonian fluid. In many cases, the understanding of viscoelastic rheology is poor. One reason is the approximate nature of the constitutive equations [1, 2]; there is no systematic way of determining the range of validity of a model in describing a specific fluid. All models are at most reasonable approximations in a limited range of flow conditions. Even if the validity of the constitutive equation is taken for granted, its mathematical complexity rarely allows the derivation of analytical results, except for the simple cases of viscoelastic flows. It is, in this context, that direct numerical simulations are called for, both to test constitutive models and as a tool to analyse and predict rheological phenomena.

The particular flow problem addressed here is a four-to-one planar contraction channel flow, widely cited in References [1, 3, 4]. This geometry is popular since it is of technological importance for the polymer processing industry and also exhibits significant flow variation with changes in fluid elasticity. The constitutive model considered here is an Oldroyd-fluid [2]. This problem manifests sufficiently complex flow phenomena and provides a challenge to the numerical algorithms and the constitutive models, in particular, for highly elastic fluid behaviour. The understanding of the problem is therefore of practical importance not only in the study of fundamental flow property behaviour but also in the application to many industries.

The planar contraction channel flow problems, over the years, have been solved by a variety of numerical techniques. Most advances have been made through the application of finite-element methods. These methods include the mixed Galerkin finite-element method [5–7], the explicitly elliptic momentum equation formulation (EEME) [8], and the elastic viscous splitting stress formulation (EVSS) [9–11]. A variety of alternative formulations have been developed during the last decade as well, for instance, streamline integration methods [12], finite-volume methods [13–15] and the hybrid finite volume and element methods [16], but these are not considered in this paper although some references are made for comparison purposes. Reviews covering these works can be found in the book of Huilgo *et al.* [17].

The mixed Galerkin finite-element methods have been the most popular approaches, and one particular approach that has been employed with considerable success is the streamline upwind stress sub-element method of Marchal and Crochet [7, 18], where the velocity field is interpolated by means of the Hermitian shape functions for satisfying an equivalence criterion between the velocity–pressure and the stress formulations. The method of EEME developed by King *et al.* [8] is based on the idea of solving an elliptic steady-state problem, which avoids a change of type to hyperbolic form by some special treatments. The advantage of the EEME method is the enforced elliptic nature in the momentum equation, which is maintained as the fluid elasticity is increased. However, the philosophy of the EEME formulation, involving a strongly elliptic momentum system and a properly represented hyperbolic constitutive equation, was accepted as a way to improve viscoelastic simulation methods. The EVSS method was first developed by Rajagopalan *et al.* [10] to generalize the EEME method and focus on constitutive models containing a purely viscous component. There are two principal features associated with this method, stress splitting and recovery of velocity gradients. This method is beneficial in maintaining the mathematical properties of the momentum and continuity problems, the proper treatment of the hyperbolic constitutive equation remains an important part of the overall algorithm. Furthermore, Rajagopalan *et al.* [10] have shown that the EVSS

method is more accurate and stable than the EEME method. Recently, Guenette and Fortin [19] have introduced a modification of the EVSS formulation, known as the discrete EVSS method (DEVSS). In this method, a stabilizing elliptic operator is introduced in the discrete version of momentum equation. This is similar to the EVSS method but the objective derivative of the rate of the deformation tensor is avoided. The reader is referred to an extensive review of Baaijens [20] on the development of the EVSS methods. The spectral element has not been used very often with non-Newtonian fluids, but there are still some works. Two recent papers adopting the spectral element approach for viscoelastic fluids are those of Chauviere *et al.* [21, 22] and Li *et al.* [23]. Chauviere *et al.* used a spectral element method to simulate a viscoelastic fluid past a cylinder in a channel, while Li *et al.* considered a non-Newtonian fluid in the journal bearing problem with the spectral element approximations.

In this study, we present a spectral element method combined with the EVSS approach based on the Gauss–Lobatto–Legendre polynomials to solve a four-to-one planar contraction channel flow with an Oldroyd-B fluid. In the spectral element method, a complex domain is decomposed into simpler domains called spectral elements, in each of which a spectral representation is used to represent each of the dependent variables. The preconditioned conjugate gradient method is used to solve the resulting system of algebraic equations. The numerical algorithm proposed in this paper does not degrade accuracy to enhance stability. Indeed, through the consistency of the approach proposed, a high degree of accuracy is afforded with the spectral approximations combined with the EVSS approach.

The structure of this paper is as follows: In Section 2, we introduce the governing system of equations and the model of an Oldroyd-B fluid, and reformulate the equations in two-dimensional Cartesian co-ordinates. In Section 3, we briefly review the spectral element approximations in the Galerkin variational formulations and present a numerical scheme based on the EVSS procedure. A discussion of the choice of the approximation function spaces for the stress and deformation tensor are also given in this section. In Section 4, we present an Uzawa algorithm to decouple the velocity from the formulation of the pressure in the momentum and continuity equations, and develop a preconditioned conjugate gradient iterative method to solve the discretization equations for the velocity, pressure, extra stress and the rate of deformation. In Section 5, we present the simulation results with an Oldroyd-B fluid through a planar four-to-one contraction channel, and show the numerical results are in good agreement with those of the other numerical predictions and the experimental measurements. A conclusion finally follows in Section 6.

2. MATHEMATICAL MODELLING

The mathematical model for viscoelastic flow involves the solution of a set of conservation and constitutive equations. For the isothermal flow of an incompressible fluid in the absence of a body force, the conservation equations for momentum and mass can be, respectively, written as

$$\rho\left(\frac{\partial \mathbf{u}}{\partial t}+\mathbf{u}\cdot\nabla\mathbf{u}\right)=-\nabla p+\nabla\cdot\boldsymbol{\tau} \tag{1}$$

$$\nabla\cdot\mathbf{u}=0 \tag{2}$$

where ρ is the fluid density, p is the pressure, $\mathbf{u}$ is the velocity vector, and $\boldsymbol{\tau}$ is the extra-stress tensor field. Equations (1) and (2) are not complete without an expression of the extra stress tensor $\boldsymbol{\tau}$. In general, a constitutive equation or (a rheological equation) is used to define such an extra stress tensor, which expresses a relationship between the stress and the velocity gradient and describes the rheology behaviour of a viscoelastic fluid. constitutive model of the integral or differential type. In this paper, a differential constitutive Oldroyd-B fluid model is used and defined as

$$\boldsymbol{\tau} + \lambda_1 \overset{\nabla}{\boldsymbol{\tau}} = 2\eta(\mathbf{D} + \lambda_2 \overset{\nabla}{\mathbf{D}}) \tag{3}$$

where λ_1 is the relaxation time, λ_2 is the retardation time and η is the shear viscosity. $\mathbf{D}$ is the rate of deformation tensor and $\overset{\nabla}{\boldsymbol{\tau}}$ is defined as an upper-convected derivative of the viscoelastic extra stress. They are defined by

$$\mathbf{D} = \tfrac{1}{2}(\nabla\mathbf{u} + (\nabla\mathbf{u})^{\mathrm{T}}) \tag{4}$$

and

$$\overset{\nabla}{\boldsymbol{\tau}} = \frac{\partial\boldsymbol{\tau}}{\partial t} + \mathbf{u}\cdot\nabla\boldsymbol{\tau} - \boldsymbol{\tau}\cdot(\nabla\mathbf{u}) - (\nabla\mathbf{u})^{\mathrm{T}}\cdot\boldsymbol{\tau} \tag{5}$$

Equation (3) is reduced to a Newtonian model when $\lambda_1 = \lambda_2 = 0$ and to the upper-convected Maxwell (UCM) model when $\lambda_2 = 0$.

Following Reference [10], the viscoelastic extra stress $\boldsymbol{\tau}$ can be split into two parts in terms of a viscous and a viscoelastic contributions

$$\boldsymbol{\tau} = \boldsymbol{\tau}_1 + \boldsymbol{\tau}_2 \tag{6}$$

where $\boldsymbol{\tau}_1$ is the elastic stress part and defined by

$$\boldsymbol{\tau}_1 + \lambda\overset{\nabla}{\boldsymbol{\tau}}_1 = 2\eta_1\mathbf{D}$$

and $\boldsymbol{\tau}_2$ denotes the viscous stress defined by

$$\boldsymbol{\tau}_2 = 2\eta_2\mathbf{D} \tag{7}$$

where $\eta = \eta_1 + \eta_2$, and η_1 is the viscosity of the viscoelastic contribution and η_2 is the viscosity of the Newtonian contribution. Substitute Equation (6) into Equation (3) and equate the coefficients of $\mathbf{D}$ and $\overset{\nabla}{\mathbf{D}}$ with $\lambda_2 = \lambda_1\eta_2/(\eta_1+\eta_2)$, we can rewrite the Oldroyd-B constitutive equation as

$$\boldsymbol{\tau}_1 + \lambda_1\overset{\nabla}{\boldsymbol{\tau}}_1 = 2\eta_1\mathbf{D} \tag{8}$$

Equations (1), (2) and (8) are completely defined for an incompressible viscoelastic flow of an Oldroyd-B fluid subject to the appropriate boundary conditions. For the problems solved in later sections, we will choose the geometry in such a way that fully developed velocity profiles can be imposed in entry and exit sections. Moreover, the extra-stress tensor $\boldsymbol{\tau}_1$ based on a fully developed flow will also be imposed at the entry section.

For numerical flow simulations, we are interested in the EVSS formulations of the problem which allows one to introduce the rate of deformation tensor [10] as an additional unknown

in order to maintain the momentum and continuity equations as a fully elliptic equation system with well-understood mathematical and numerical properties. A change of variables is introduced with

$$\mathbf{d} = \mathbf{D} = \tfrac{1}{2}(\nabla \mathbf{u} + (\nabla \mathbf{u})^{\mathrm{T}}) \tag{9}$$

and

$$\mathbf{S} = \boldsymbol{\tau}_1 - 2\,\eta_1 \mathbf{d} \tag{10}$$

Substituting (9) and (10) into the momentum equation (1) and using the expression

$$\nabla \cdot \mathbf{S} = \nabla \cdot \boldsymbol{\tau}_1 - 2\,\eta_1 \nabla \cdot \mathbf{d}$$

yields the following momentum, continuity and constitutive equations

$$\rho\left(\frac{\partial \mathbf{u}}{\partial t} + \mathbf{u} \cdot \nabla \mathbf{u}\right) = -\nabla p + \nabla \cdot \boldsymbol{\tau} - 2\,\eta_1 \nabla \cdot \mathbf{d} + 2\,\eta \nabla \cdot \mathbf{D} \tag{11}$$

$$\nabla \cdot \mathbf{u} = 0 \tag{12}$$

$$\boldsymbol{\tau} + \lambda_1 \overset{\nabla}{\boldsymbol{\tau}} = 2\,\eta_1 \mathbf{D} \tag{13}$$

where

$$\mathbf{d} = \mathbf{D} \tag{14}$$

Note that $\boldsymbol{\tau}_1$ has been replaced by $\boldsymbol{\tau}$ in these equations. Although we have added the same quantity to both sides of the momentum equation, the real modification will appear when we consider a different representation for $\mathbf{d}$ and $\mathbf{D}$ in the discrete form of the above system of equations which will be solved in a different discrete function space. If the exact solution is recovered, Equation (14) vanishes. However, in a finite-element calculation this is generally not the case [20]. It must be emphasized that the stress splitting formulations are beneficial in maintaining the mathematical elliptic properties of the momentum and continuity equations, but the proper treatment of the hyperbolic constitutive equation remains an important part of the overall algorithm.

We now rewrite Equations (11)–(14) in component forms assuming two-dimensional flow in Cartesian co-ordinates

$$\rho\left(\frac{\partial u_i}{\partial t} + u_j \frac{\partial u_i}{\partial x_j}\right) = -\frac{\partial p}{\partial x_j} + \frac{\partial \tau_{ij}}{\partial x_j} - 2\,\eta_1 \frac{\partial d_{ij}}{\partial x_j} + \eta \frac{\partial^2 u_i}{\partial x_j^2} \tag{15}$$

$$\frac{\partial u_i}{\partial x_i} = 0 \tag{16}$$

$$\tau_{ij} + \lambda_1\left(\frac{\partial \tau_{ij}}{\partial t} + u_l \frac{\partial \tau_{ij}}{\partial x_l}\right) = \eta_1\left(\frac{\partial u_i}{\partial x_j} + \frac{\partial u_j}{\partial x_i}\right) + \lambda_1\left(\tau_{il}\frac{\partial u_j}{\partial x_l} + \tau_{jl}\frac{\partial u_i}{\partial x_l}\right) \tag{17}$$

$$d_{ij} = \frac{1}{2}\left(\frac{\partial u_i}{\partial x_j} + \frac{\partial u_j}{\partial x_i}\right), \quad \forall i, j, l = 1, 2 \tag{18}$$

Dimensionless variables are then introduced

$$x^* = \frac{x}{L}, \quad y^* = \frac{y}{L}, \quad u_i^* = \frac{u_i}{U}, \quad t^* = \frac{Ut}{L}, \quad p^* = \frac{Lp}{\eta U}, \quad \tau_{ij}^* = \frac{L}{\eta U}\tau_{ij}, \quad d_{ij}^* = \frac{L}{U}d_{ij}$$

where U is a characteristic velocity and L is a characteristic length. Substituting these expressions into (15)–(18), dropping the symbol $*$ and rearranging the resulting equations gives the following dimensionless system of equations:

$$Re\left(\frac{\partial u_i}{\partial t} + u_j\frac{\partial u_i}{\partial x_j}\right) = -\frac{\partial p}{\partial x_j} + \frac{\partial \tau_{ij}}{\partial x_j} - 2(1-\beta)\frac{\partial d_{ij}}{\partial x_j} + \frac{\partial^2 u_i}{\partial x_j^2} \tag{19}$$

$$\frac{\partial u_i}{\partial x_i} = 0 \tag{20}$$

$$\tau_{ij} + We\left(\frac{\partial \tau_{ij}}{\partial t} + u_l\frac{\partial \tau_{ij}}{\partial x_l}\right) = (1-\beta)\left(\frac{\partial u_i}{\partial x_j} + \frac{\partial u_j}{\partial x_i}\right) + We\left(\tau_{il}\frac{\partial u_j}{\partial x_l} + \tau_{jl}\frac{\partial u_i}{\partial x_l}\right) \tag{21}$$

$$d_{ij} = \frac{1}{2}\left(\frac{\partial u_i}{\partial x_j} + \frac{\partial u_j}{\partial x_i}\right), \quad \forall i,j,l = 1,2 \tag{22}$$

where $\beta = \lambda_2/\lambda_1$ determines the characteristics of the Oldroyd-B fluid; $Re = \rho UL/\eta$ is the Reynolds number, which expresses the ratio of the inertia forces to the viscous forces; $We = \lambda_1 U/L$ is the Weissenberg number, which determines the elastic character of the fluid. Notice that high values of We indicate a material response that is very solid-like, while low values of the parameter represent small departures from normal viscous fluid behaviour.

3. THE SPECTRAL ELEMENT METHOD

In this study, the spectral element method is chosen for the spatial discretization of the system of equations given in the previous section. In the spectral element method, a complex domain is decomposed into simpler domains called spectral elements, in each of which a spectral representation is used to represent each of the dependent variables. The spectral element approach was first presented in Reference [24], and an excellent review was given by Maday and Patera [25]. This method, like the spectral method, uses high-order polynomials as trial functions, and like the finite-element method, decomposes the computational domain into a number of simpler domains on which local trial functions are defined. The hybrid character of the spectral element method enables it to overcome the shortcomings of both the spectral method and the finite-element method but still retain their advantages. Since the trial functions of the spectral element method are local, the method can handle complex geometries easily. On the other hand, it is still a high-order weighted residual method, so the exponential convergence rate is achieved as the degree of the polynomial approximation in each element is increased [25]. In the following sections, a spectral element algorithm will be presented with the EVSS method based on the model of an Oldroyd-B fluid.

3.1. *Variational formulation*

In order to pose a weak formulation equivalent to the system of Equations (19)–(22), we first introduce the following function spaces:

$$V_0(\Omega) = \{\phi \in H_0^1(\Omega)\} \tag{23}$$

$$Q_0(\Omega) = \left\{ p \in L^2(\Omega) \text{ and } \int_\Omega p \, \mathrm{d}\Omega = 0 \right\} \tag{24}$$

where $H_0^1(\Omega)$ denotes the subspace of $H^1(\Omega)$ of functions which are zero on the boundary

$$H_0^1(\Omega) = \{\phi \in H^1(\Omega),\ \phi = 0 \text{ on } \Gamma\}$$

Let $V(\Omega)$ and $Q(\Omega)$ denote the spaces

$$V(\Omega) = H^1(\Omega) = \{\phi \in L^2(\Omega);\ \nabla\phi \in L^2(\Omega)\}$$
$$Q(\Omega) = \{\phi \in L^2(\Omega)\}$$

where $L^2(\Omega)$ is the space of square integrable functions. The scalar product can be defined as

$$(\phi, \psi) = \int_\Omega \phi(x)\psi(x) \, \mathrm{d}x, \quad \forall \phi, \psi \in H^1(\Omega)$$

For the sake of simplicity, we choose, without loss of generality, the velocity field equal to zero on Γ. After multiplying (19) by the weighting function $\bar{u}_i \in V_0(\Omega)$, (20) by $q \in Q_0(\Omega)$, (21) by $\bar{\tau}_{ij} \in V(\Omega)$ and (22) by $\bar{d}_{ij} \in Q(\Omega)$, and integrating by parts, we get the following variational formulation for (19)–(22) as

Find $(u_i, p, \tau_{ij}, d_{ij}) \in (V_0 \times Q_0 \times V \times Q)$ such that

$$\left(\frac{\partial u_i}{\partial x_j}, \frac{\partial \bar{u}_i}{\partial x_j}\right) + Re\left(\frac{\partial u_i}{\partial t}, \bar{u}_i\right) - \left(p, \frac{\partial \bar{u}_i}{\partial x_i}\right)$$
$$= \left(\frac{\partial \tau_{ij}}{\partial x_j}, \bar{u}_i\right) + 2(1-\beta)\left(\frac{\partial d_{ij}}{\partial x_j}, \bar{u}_i\right) - Re\left(u_j \frac{\partial u_i}{\partial x_j}, \bar{u}_i\right), \quad \forall \bar{u}_i \in V_0(\Omega) \tag{25}$$

$$\left(\frac{\partial u_i}{\partial x_j}, q\right) = 0, \quad \forall q \in Q_0(\Omega) \tag{26}$$

$$We\left(\frac{\partial \tau_{ij}}{\partial t} + u_l \frac{\partial \tau_{ij}}{\partial x_l}, \bar{\tau}_{ij}\right) + (\tau_{ij}, \bar{\tau}_{ij}) - We\left(\tau_{il} \frac{\partial u_j}{\partial x_l} + \tau_{jl} \frac{\partial u_i}{\partial x_l}, \bar{\tau}_{ij}\right)$$
$$= (1-\beta)\left(\frac{\partial u_i}{\partial x_j} + \frac{\partial u_j}{\partial x_i}, \bar{\tau}_{ij}\right), \quad \forall \bar{\tau}_{ij} \in V(\Omega) \tag{27}$$

$$\left(d_{ij}, \bar{d}_{ij}\right) = \frac{1}{2}\left(\frac{\partial u_i}{\partial x_j} + \frac{\partial u_j}{\partial x_i}, \bar{d}_{ij}\right), \quad \forall \bar{d}_{ij} \in Q(\Omega) \tag{28}$$

Under certain conditions, one can prove that there exists a unique solution $(u_i, p, \tau_{ij}, d_{ij})$ to the variational formulation (25)–(28), the details can be found in References [5, 26].

3.2. Spatial discretization

Consider the numerical solution of the weak formulation (25)–(28) in a domain Ω using the spectral element method. The domain Ω is divided into a number of non-overlapping spectral elements, Ω_k, $k=1,\ldots,K$, such that $\Omega=\bigcup\Omega_k$ and $\Omega_k\cap\Omega_l=\emptyset$, $\forall k,l,k\neq l$. Each spectral element Ω_k is mapped onto the parent element $\chi=[-1,1]\times[-1,1]$. The mapping is usually performed using an isoparametric or transfinite mapping. Therefore, we may associate with each point $(\xi,\eta)\in\chi$ a unique point $(x,y)\in\Omega_k$.

With the above decomposition of Ω, the discretization of (23) and (24) calls for the definition of subspaces

$$V_{h0}\subset V_0,\quad V_h\subset V,\quad Q_{h0}\subset Q_0,\quad Q_h\subset Q$$

In the sequel, the discretization of the variational formulations (25)–(28) can be rewritten as

Find $(u_{ih}, p_h, \tau_{ijh}, d_{ijh})\in(V_{h0}\times Q_{h0}\times V_h\times Q_h)$, such that

$$\left(\frac{\partial u_{i,h}}{\partial x_j},\frac{\partial\bar{u}_i}{\partial x_j}\right)_h+Re\left(\frac{\partial u_{i,h}}{\partial t},\bar{u}_i\right)_h-\left(p_h,\frac{\partial\bar{u}_i}{\partial x_j}\right)_h=\left(\frac{\partial\tau_{ij,h}}{\partial x_j},\bar{u}_i\right)_h$$
$$-2(1-\beta)\left(\frac{\partial d_{ij,h}}{\partial x_j},\bar{u}_i\right)_h-Re\left(u_{j,h}\frac{\partial u_{i,h}}{\partial x_j},\bar{u}_i\right)_h \tag{29}$$

$$\left(\frac{\partial u_{i,h}}{\partial x_i},q\right)_h=0 \tag{30}$$

$$We\left(\frac{\partial\tau_{ij,h}}{\partial t}+u_{l,h}\frac{\partial\tau_{ij,h}}{\partial x_l},\bar{\tau}_{ij}\right)_h-We\left(\tau_{il,h}\frac{\partial u_{j,h}}{\partial x_l}+\tau_{jl,h}\frac{\partial u_{i,h}}{\partial x_l},\bar{\tau}_{ij}\right)_h$$
$$+\left(\tau_{ij,h},\bar{\tau}_{ij}\right)_h=(1-\beta)\left(\frac{\partial u_{i,h}}{\partial x_j}+\frac{\partial u_{j,h}}{\partial x_i},\bar{\tau}_{ij}\right)_h \tag{31}$$

$$(d_{ij,h},\bar{d}_{ij})_h=\frac{1}{2}\left(\frac{\partial u_{i,h}}{\partial x_j}+\frac{\partial u_{j,h}}{\partial x_i},\bar{d}_{ij}\right)_h \tag{32}$$

$$\forall\bar{u}_i\in V_{h0},\quad q\in Q_{h0},\quad\bar{\tau}_{ij}\in V_h,\quad\bar{d}_{ij}\in Q_h$$

where

$$(f,g)_h=\sum_{k=1}^{K}\int_{\Omega_k}fg\,\mathrm{d}\Omega_k$$

In order to set up the spectral element discretization, it is necessary to choose a simple basis to span a proper functional space for the numerical approximations. In the present work, we use the Gauss–Lobatto–Legendre polynomials as a basis of the approximation space:

$$h_i(\xi) = -\frac{(1-\xi^2)L'_N(\xi)}{N(N+1)L_N(\xi_i)(\xi-\xi_i)} \quad (i=0,1,\ldots,N) \tag{33}$$

where L_N is the Nth-order Legendre polynomial, L'_N is the first-order derivative and the collocation points, ξ_i, are given by

$$-1=\xi_0<\xi_1<\cdots<\xi_N=1, \quad \forall i\in\{1,\ldots,N-1\}, \quad L'_N(\xi_i)=0 \tag{34}$$

From the definition of $h_i(\xi)$, we obtain

$$h_i(\xi_j)=\delta_{ij}, \quad \forall i,j\in\{0,\ldots,N\}$$

where δ_{ij} is the Kronecker-delta symbol. There also exists a unique set of positive real numbers w_i, corresponding to ξ_i, $(0\leqslant i\leqslant N)$, such that the integration rule

$$\int_{-1}^{1}\psi(x)\,\mathrm{d}x=\sum_{i=0}^{N}w_i\psi(\xi_i) \tag{35}$$

is exact for all polynomials $\psi(x)$ of degree $\leqslant(2N-1)$ on the interval $[-1,\ 1]$. Note that one advantage of using the Gauss–Lobatto–Legendre polynomials as basis functions is that we only have to deal with one set of grid points for interpolation and numerical quadrature.

Now we describe how we set up the spectral element approximation for the variational problem (29)–(32). Let us denote by $\mathscr{P}_{N,K}$ the space of all polynomials of degree N or less defined over each parent element χ, and choose the velocity field in $V_{h0}=H_0^1(\Omega)\cap\mathscr{P}_{N,K}$ and construct a Gauss–Lobatto–Legendre grid in the parent element χ, we can expand the velocity field in tensor product form

$$\mathbf{u}_h^k(\xi,\zeta)=\sum_{i=0}^{N_\xi}\sum_{j=0}^{N_\zeta}\mathbf{u}_{i,j}^k h_i(\xi)h_j(\zeta) \tag{36}$$

where $\mathbf{u}_{ij}^k=\mathbf{u}_h^k(\xi_i^k,\zeta_j^k)$ is the velocity at the Gauss–Lobatto–Legendre point (ξ_i^k,ζ_j^k) in the sub-domain Ω_k, and $(x,y)\in\Omega_k\rightarrow(\xi,\zeta)\in\chi$. Here N_ξ and N_ζ represent the numbers of collocation points in each of the spatial directions.

As for the finite-element method, the velocity and pressure spaces must satisfy the Babuŝka–Brezzi inf–sup compatibility condition in order to have a solvable system leading to a pressure field that is not polluted by spurious pressure wiggles. In the framework of the spectral element method, Maday *et al.* [25] have shown that a suitable choice for the pressure approximation space is

$$Q_{h0}=Q_0(\Omega)\cap\mathscr{P}_{N-2,K}$$

With this choice of the pressure approximation space, the dimension of Q_{h0} is only $K(N-1)^2$ since function continuity is not enforced for functions in Q_{h0}. However, the dimension of V_{h0} is less than $K(N+1)^2$ due to the restriction that functions in V_{h0} must be continuous across sub-domain interfaces and must also satisfy Dirichlet boundary conditions on $\partial\Omega$. With such a choice of the pressure and velocity approximation spaces the inf–sup compatibility condition

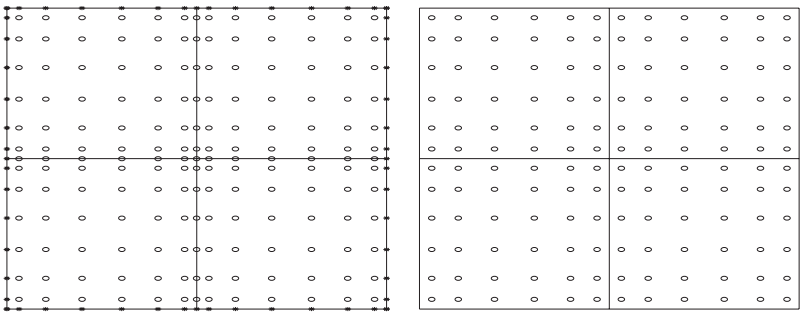

Figure 1. A typical spectral element configuration: there are four elements in each picture, and eight collocation points are chosen in both x and y directions. The velocity and extra stress are defined on the Gauss–Lobatto–Legendre collocation points shown in the left figure, the pressure and the rate of deformation tensor are defined on the interior Gauss–Lobatto–Legendre points shown in the right figure, where ○ denotes the interior nodes, while • denotes the boundary nodes.

is satisfied [25]. Furthermore, it has been shown both numerically and theoretically that the spectral element solution to the Stokes problem convergences exponentially as $N \to \infty$ for problems having smooth solutions [25].

Therefore, we choose the pressure function in the space Q_{h0} and expand it on the interior Gauss–Lobatto–Legendre points. Thus, the pressure approximation can be written as

$$p_h^k(\xi,\zeta) = \sum_{i=1}^{N_\xi - 1} \sum_{j=1}^{N_\zeta - 1} p_{ij}^k \bar{h}_i(\xi)\bar{h}_j(\zeta) \tag{37}$$

where $p_{ij}^k = p(\xi_i^k, \zeta_j^k)$ is the pressure at the interior Gauss–Lobatto–Legendre points in Ω_k, and $\bar{h}_i$ is defined by

$$\bar{h}_i(\xi) = -\frac{(1-\xi_i^2)L_N'(\xi)}{N(N+1)L_N(\xi_i)(\xi-\xi_i)}$$
$$\xi \in [-1,1], \quad \forall i \in \{1,\ldots,N-1\}$$

Figure 1 shows the nodal points for both the velocity and the pressure meshes for a regular sub-domain configuration. Note that the basis for velocity is continuous across sub-domain interfaces, while the basis for the pressure is not.

Another important aspect of the discretization of viscoelastic flow problems by the spectral element method (or the finite-element method) is the choice of approximation space for the extra-stress tensor, since the extra-stress fields for a viscoelastic fluid are generally more complex than their corresponding velocity counterparts. In the velocity–pressure–stress formulations, Gerritsma *et al.* [27] have shown that a second compatibility condition between the discrete velocity and the extra-stress approximation is required and have also shown that the problem is well posed provided one chooses the stress approximation space to contain polynomials of at least the same degree as the velocity space. Hence, a simple choice of the extra-stress space is V_h. With this choice the extra-stress approximation can be written as

$$\boldsymbol{\tau}_h^k(\xi,\zeta) = \sum_{i=0}^{N_\xi} \sum_{i=0}^{N_\zeta} \boldsymbol{\tau}_{ij}^k h_i(\xi) h_j(\zeta) \tag{38}$$

where $\boldsymbol{\tau}_{ij}^k = \boldsymbol{\tau}(\xi_i^k, \zeta_j^k)$. It should be noted that there are many ways of choosing the extra-stress approximation function spaces, but we make no comments here about their relative merits since it is beyond the scope of this paper.

The choice of the function spaces for the deformation tensor $d_{ij,h}$ can be made in different ways. For example, if $d_{ij,h} \in \nabla V_h$, one can substitute $d_{ij,h}$ into (29) and obtain a classical discrete formulation for the Oldroyd-B problem due to $\mathbf{d} \equiv \mathbf{D}$ in (32). In general, the deformation space should not be rich enough to fully represent any element in ∇V_h, (see Reference [10]). In essence, guidance is still often lacking as to what kind of interpolations for the rate of deformation are admissible. In this paper, we follow [10] and choose the rate of deformation tensor approximation space expanded by the polynomials of the same degree as the pressure space, namely,

$$Q_h = Q(\Omega) \cap \mathscr{P}_{N-2,K}$$

In this definition, the rate of deformation tensor approximation can be expanded in the form

$$\boldsymbol{d}_h^k(\xi, \zeta) = \sum_{i=1}^{N_\xi - 1} \sum_{j=1}^{N_\zeta - 1} \boldsymbol{d}_{ij}^k \bar{h}_i(\xi) \bar{h}_j(\zeta) \tag{39}$$

where $\boldsymbol{d}_{ij}^k = \boldsymbol{d}(\xi_i^k, \zeta_j^k)$.

Figure 1 shows the spectral element configurations, in which the velocity and stress are chosen at the Gauss–Lobatto–Legendre collocation points, while the pressure and the rate of deformation tensor are chosen at the interior Gauss–Lobbato–Legendre points. It is worth pointing out that the above choice of the approximation spaces for the velocity and extra stress (and also for the pressure and the rate of deformation tensor) has obvious advantages from the point of view of implementation on the computing program because no interpolations are required between the velocity and extra stress grids. Of course, there are no interpolations required between the pressure and the rate of deformation tensor grids as well.

We now insert the velocity, pressure, extra stress and the rate of deformation tensor approximations (36)–(39) into Equations (29)–(32) and the discrete equations are generated by choosing appropriate test functions $\bar{u}_i \in V_{h0}$ and $\bar{\tau}_{ij} \in V_h$, whose values at the point (ξ_i, ζ_j) are unity and zero at all other Gauss–Lobatto–Legendre points, and test functions $q \in Q_{h0}$ and $\bar{d}_{ij} \in Q_h$, whose values are unity at the point (ξ_i, ζ_j) and zero at all other interior Gauss–Lobatto–Legendre points. In this way, we obtain the discretizational system of equations

$$A\mathbf{u} - D^{\mathrm{T}} p = f \tag{40}$$

$$-D \cdot \mathbf{u} = 0 \tag{41}$$

$$C\boldsymbol{\tau} = g \tag{42}$$

$$E\mathbf{d} = h \tag{43}$$

where A is the discrete Helmholtz operator, D is the discrete gradient operator, C is the stress tensor matrix, E is the deformation tensor matrix and f, g and h are the right-hand side vectors, which are incorporated with boundary conditions.

It should be noted that in Equations (40)–(43) the linear operator, such as the second-order viscous operator, is treated by an implicit approach, while the non-linear operator, such as an

inertia term, is conveniently treated in an explicit fashion. And the first-order derivatives $\partial/\partial t$ in Equations (29) and (31) are calculated by the first-order backward Euler time marching scheme. Of course, other temporal discrete schemes can be used here. For the technical details of the implementation of the temporal discrete schemes, the reader is referred to Reference [28].

4. THE UZAWA ITERATIVE METHOD

In this section, the Uzawa procedure will be used to decouple the pressure and velocity computations [29]. In this way, a saddle point problem will be replaced by two symmetric positive (semi)-definite systems [30].

We begin with a decoupling of the original problem (40)–(41) into two positive semi-definite symmetric forms, one for the velocity $\mathbf{u}$ and one for the pressure p. First, for each of the velocity components u_i from the momentum equations, we formally solve

$$u_i = A^{-1} D_i^{\mathrm{T}} p + A^{-1} f_i, \quad i = 1, 2 \tag{44}$$

We then substitute (44) into the continuity equation (41) to obtain the following equation for the pressure:

$$(D_1 A^{-1} D_1^{\mathrm{T}} + D_2 A^{-1} D_2^{\mathrm{T}}) p - (D_1 A^{-1} f_1 + D_2 A^{-1} f_2) = 0 \tag{45}$$

Hence, the conservation equations (40) and (41) can be recast into the following equivalent equations for the velocity and pressure:

$$A u_i = D_i^{\mathrm{T}} p + f_i, \quad i = 1, 2 \tag{46}$$

$$S p = G \tag{47}$$

where the discrete pressure matrix is

$$S = D_1 A^{-1} D_1^{\mathrm{T}} + D_2 A^{-1} D_2^{\mathrm{T}} \tag{48}$$

which is symmetric positive definite and

$$G = -(D_1 A^{-1} f_1 + D_2 A^{-1} f_2) \tag{49}$$

We make several observations about these matrices. First of all, since matrices A and S are symmetric and positive (or semi)-definite, standard elliptic solvers, such as the conjugate gradient iteration technique, can readily be applied. Secondly, since the velocity and pressure in Equations (46) and (47) are completely decoupled in the solution process, we can first solve Equation (47) for the pressure p and then solve Equation (46) for each velocity component u_i with p known. Similarly, we can solve Equations (42) and (43), with u_i known, for the components of the stress τ_{ij} and the rate of deformation d_{ij}, respectively. Finally, it should be noted that the pressure matrix S is completely full due to the embedded inverse of A, and, therefore, a nested iterative approach proposed in Reference [25] is required to solve Equation (47).

Using the preconditioned conjugate gradient method (PCG) to solve this system is well documented in references (see References [24, 25]) and suitable preconditioners have been advocated which yield efficient numerical algorithms. In this paper, we use a preconditioner, which changes dynamically in time, taking into account the number of PCG iterations required for convergence at each time step for the current Weissenberg number. The preconditioner is based on the pressure matrix evaluated at a given Weissenberg number. Further details regarding the choice of preconditioners can be found in Reference [25].

Finally, the numerical procedure proposed in this paper can be summarised as follows:

- given an initial approximation of $(\boldsymbol{u}^0, p^0, \boldsymbol{\tau}^0, \boldsymbol{d}^0)$;
- determine the velocity $\boldsymbol{u}^n$ and the pressure p^n by solving Equations (46) and (47) with $\boldsymbol{\tau}^{n-1}$ and $\boldsymbol{d}^{n-1}$ known;
- determine the stress $\boldsymbol{\tau}^n$ by solving Equation (42) with $\boldsymbol{u}^n$ known;
- determine the rate of deformation tensor $\boldsymbol{d}^n$ by solving Equation (43) with $\boldsymbol{u}^n$ known;
- recalculate all variables again and stop when a steady-state solution is obtained.

5. RESULTS AND DISCUSSION

A standard test problem for the study of viscoelastic flow behaviour is the entry flow in a symmetric planar contraction channel. This geometry is popular since it is of technological importance for the polymer processing industry and also exhibits significant flow variation with changes in fluid elasticity. In this paper, we consider a fully developed Poiseuille flow through a channel with an abrupt symmetric four-to-one contraction. The difficulty of the contraction problem is that a singular solution exists, which is caused by the geometric singularity at the re-entrant corner. As the fluid elasticity is increased, such a singularity becomes stronger in the viscoelastic flow than that in the Newtonian flow [31]. This may be the reason behind its choice as a benchmark problem in the non-Newtonian flows.

Figure 2 shows a schematic diagram of a fully developed Poiseuille flow through the abrupt four-to-one contraction channel. Since the geometry is assumed to be symmetric about the centre line $y = 0$, it is only needed to consider the lower half of the channel. In this paper, the height of the outflow half channel is taken as the unit, i.e. $L = 1.0$, (the characteristic length) and the height of inflow channel is taken to be $H = 4L$, so the ratio is $a = \frac{1}{4}$. The length of the inflow channel is equal to the length of the outflow channel, and it is taken to be 16 in this paper. The Oldroyd-B fluid with $\beta = 1/9$ is chosen to be a viscoelastic model.

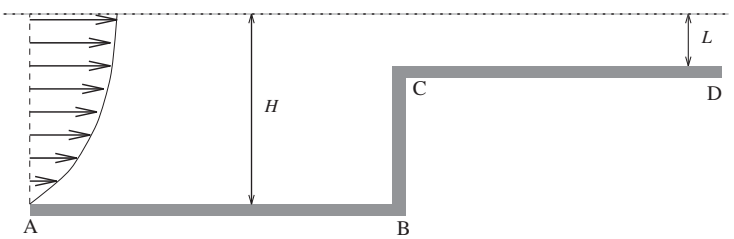

Figure 2. Schematic diagram of 4 : 1 planar contraction channel flow geometry.

Table I. Velocity boundary conditions.

Inflow	$u = \frac{3}{128}(16 - y^2)$
	$v = 0$
Outflow	$u = \frac{3}{2}(1 - y^2)$
	$v = 0$
Boundary parallel to x-axis	$u = 0$
	$v = 0$
Boundary parallel to y-axis	$u = 0$
	$v = 0$
Axis of symmetry	$v = 0$
	$\partial u/\partial y = 0$

Table II. Stress boundary conditions.

Inflow	$\tau_{xx} = 2\,We(1 - \beta)(\partial u/\partial y)^2$
	$\tau_{yy} = 0$
	$\tau_{xy} = (1 - \beta)\partial u/\partial y$
Boundary parallel to x-axis	$\tau_{xx} = 2\,We(1 - \beta)(\partial u/\partial y)^2$
	$\tau_{yy} = 0$
	$\tau_{xy} = (1 - \beta)\partial u/\partial y$
Boundary parallel to y-axis	$\tau_{xx} = 0$
	$\tau_{yy} = 2\,We(1 - \beta)(\partial v/\partial x)^2$
	$\tau_{xy} = (1 - \beta)\partial v/\partial x$
Axis of symmetry	$\tau_{xy} = 0$

In this paper, we impose a fully developed Poiseuille flow at the inlet and outlet boundaries in order to ensure the mass is conserved in a discrete sense, and the no-slip conditions $u = v = 0$ are also applied on the solid wall. We assume that the flow field is symmetric about the x-axis; hence, the boundary conditions for the velocity should be $v = 0$ and $\partial u/\partial y = 0$ on the central line. The details of the velocity boundary conditions are shown in Table I.

The boundary conditions for the stresses along the solid wall and inlet are derived from the steady-state constitutive equations which are shown in Table II. At the exit the stress boundary conditions are defined as

$$\frac{\partial \tau_{xx}}{\partial x} = \frac{\partial \tau_{yy}}{\partial x} = \frac{\partial \tau_{xy}}{\partial x} = 0 \tag{50}$$

To illustrate numerical simulations for the symmetric planar contraction channel flow the spectral element method combined with EVSS approach proposed in the previous section is employed. Based on the geometry shown in Figure 2, two different meshes, depicted in Figures 3 and 4 are used in the spectral element approximations. Figure 3 shows Mesh I which is five elements, on each element there are 13×5 collocation points in the x and y directions, respectively. Figure 4 shows Mesh II in which there are three elements with 19×7 collocation points in the x and y directions, respectively, on each element. Characteristic data of these meshes are listed in Table III, which indicates the total number of degrees of freedom

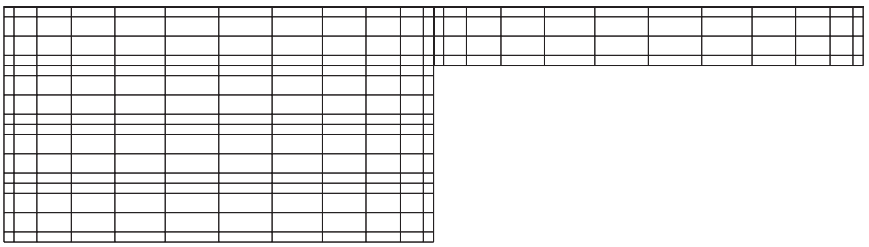

Figure 3. Spectral element mesh generation: *Mesh I*.

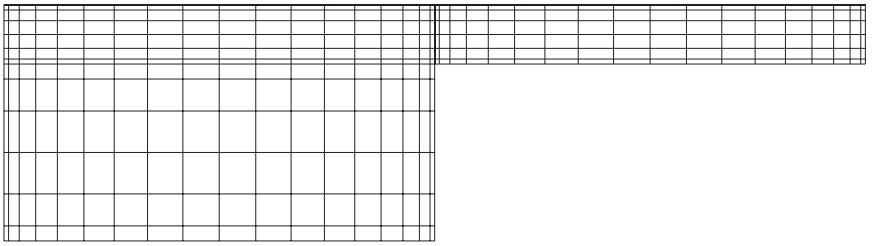

Figure 4. Spectral element mesh generation: *Mesh II*.

Table III. Spectral element mesh characteristic data.

Degree of freedom	Mesh I	Mesh II
velocity	281	373
extra stress tensor	281	373
pressure	165	255
deformation tensor	165	255
Size of corner element $x \times y$	0.373×0.172	0.171×0.085

for the velocity, pressure, extra stress and deformation tensors. The mesh is concentrated on the corner where the smallest rectangles are 0.373×0.172 for Mesh I and 0.171×0.085 for Mesh II. In a time-dependent simulation, the steady-state solution is supposed to be attained when residuals of the velocity and stress become smaller than some appropriate criterion. In this paper, we choose such a value as 10^{-5}, a smaller tolerance provides no further insight into the method. It should be noted that the present simulations are explicitly time dependent so that steady-state convergence is dependent on the physical phenomena and independent of the size of time steps, though the total computing time varies with the time steps.

We first validate the spectral element algorithm with a Newtonian flow, i.e. $\lambda_1 = 0$ and compare the quality of the numerical solutions on the Meshes I and II at $Re = 1$. Figures 5 and 6 show the flow streamlines on Meshes I and II, respectively. Here we find agreement on two meshes, hence, convergence with mesh refinement is confirmed. Figures 7 and 8 show the contours of the velocity component u with Meshes I and II, respectively. These contour plots indicate that there are no significant differences observed on the solutions or convergence patterns between the use of the two meshes. Hence, Mesh I has been used throughout unless stated otherwise.

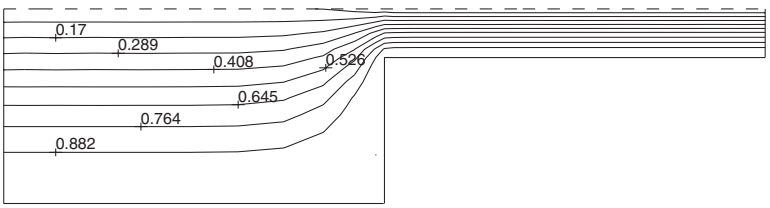

Figure 5. Streamlines for the Newtonian flow with *Mesh I*.

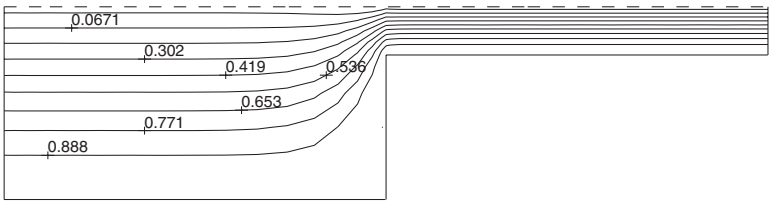

Figure 6. Streamlines for the Newtonian flow with *Mesh II*.

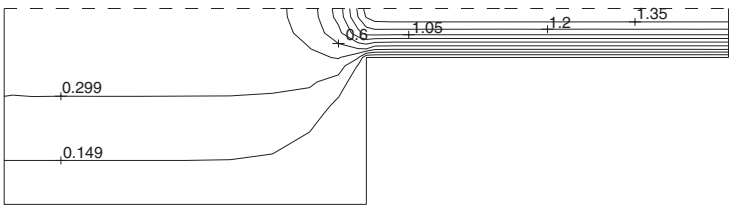

Figure 7. Contour plot of the velocity component u for the Newtonian fluid with Mesh I.

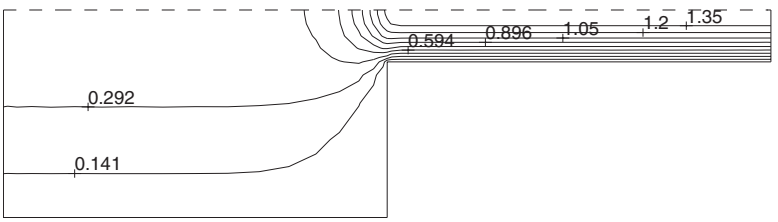

Figure 8. Contour plot of the velocity component u for the Newtonian fluid with Mesh II.

Now we use the spectral element approximations to simulate flow through the four-to-one planar contraction channel with the Oldroyd-B fluids according to the values of the Weissenberg number We in the analysis. First, the streamlines are plotted in Figure 9 for $We = 0.1, 0.4, 0.8$ and 1.2, respectively, at $Re = 1.0$. By inspection of Figure 9, we are able to see that the size of the vortex corner is diminished when the Weissenberg number increases. Here, the salient corner vortices do not reflect significant vortex enhancement. Including inertia

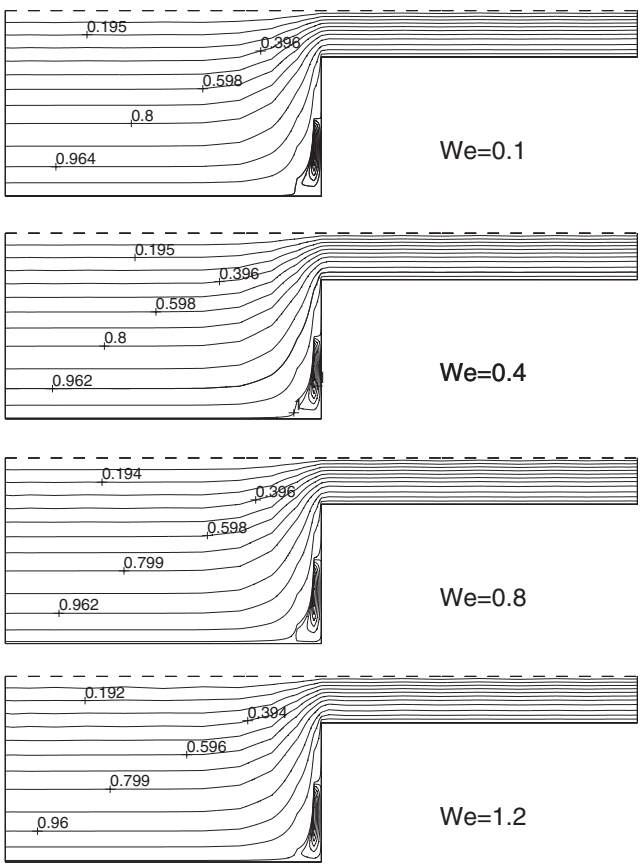

Figure 9. Streamline comparisons with increasing We at $Re = 1.0$.

($Re = 1.0$) has the effect of pushing the salient corner vortex into the corner recess and the onset of a lip vortex is delayed. This phenomena has been observed in the experimental measurements for planar contraction flows by Walters *et al.* [32], where they found that the corner vortex slightly diminishes in size when We increases for a Boger fluid, which is often identified with an Oldroyd-B fluid because it is non-shear thinning. Hence, the present numerical simulations shown in Figure 9 are consistent with the experimental observations within a range of We similar to their flow visualizations.

To investigate the influence of the Weissenberg numbers on the pattern of the streamlines, the cell vortex size determined by the parameters of l_x and l_y is presented in Table IV with different We, where l_x denotes the distance from the salient corner to the point where the separation line reaches the wall parallel to the x-axis, and l_y denotes the distance from the salient corner to the point where the separation line reaches the wall parallel to the y-axis. It is clearly shown that when We increases from 0 to 0.6, the length of the corner vortex, l_x, remains constant, while the width of the corner vortex, l_y, increases. But when We increases from 0.7 to 1.2, l_x decreases slightly, while l_y remains constant. To compare with published results, the cell vortex size is plotted as a function of the number of We in

Table IV. Values of l_x, l_y and $\varphi_{\max}$ for various We numbers with Mesh I.

We	l_x	l_y	$\varphi_{\max}$
0.1	1.3093	1.086	1.0010672
0.2	1.3093	1.108	1.0010955
0.3	1.3093	1.129	1.0011469
0.4	1.3093	1.140	1.0011860
0.5	1.3093	1.151	1.0012160
0.6	1.3093	1.151	1.0012207
0.7	1.229	1.162	1.0012093
0.8	1.229	1.173	1.0012238
0.9	1.229	1.173	1.0012011
1.0	1.229	1.173	1.0011356
1.1	1.176	1.173	1.0010624
1.2	1.176	1.173	1.0009739

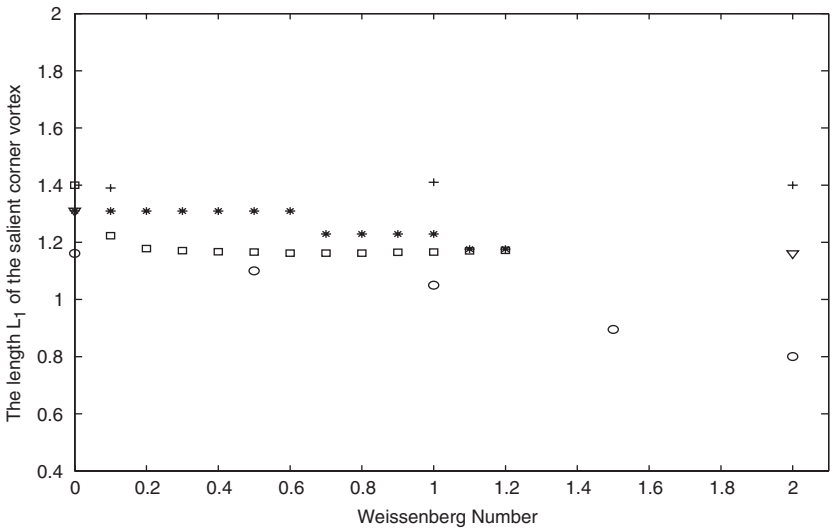

Figure 10. The size of the length l_x as function of We, where $*$ is the spectral element approximation; $\square$ by Williams [14, 15]; $\triangledown$ by Matallah [33]; $\circ$ by Sato *et al.* [35]; $+$ by Carew *et al.* [34].

Figure 10. It is shown that the behaviour of the spectral element solutions is comparable to the observations of Matallah [33] and Williams [14, 15]; however, somewhat different from the results of Carew [34] and Sato [35]. In the results of the present simulations, it is found that the maximum values of the stream functions are nearly independent of We when $0 \leqslant We \leqslant 1.2$. This is shown in Table IV. However, the minimum values of the stream function decrease when We is increased. From the numerical calculations, it is found that when $We = 0.1$, the minimum value of the stream function is $\phi_{\min} = -0.0066$, while it is $\phi_{\min} = -0.0107$, when $We = 1.2$.

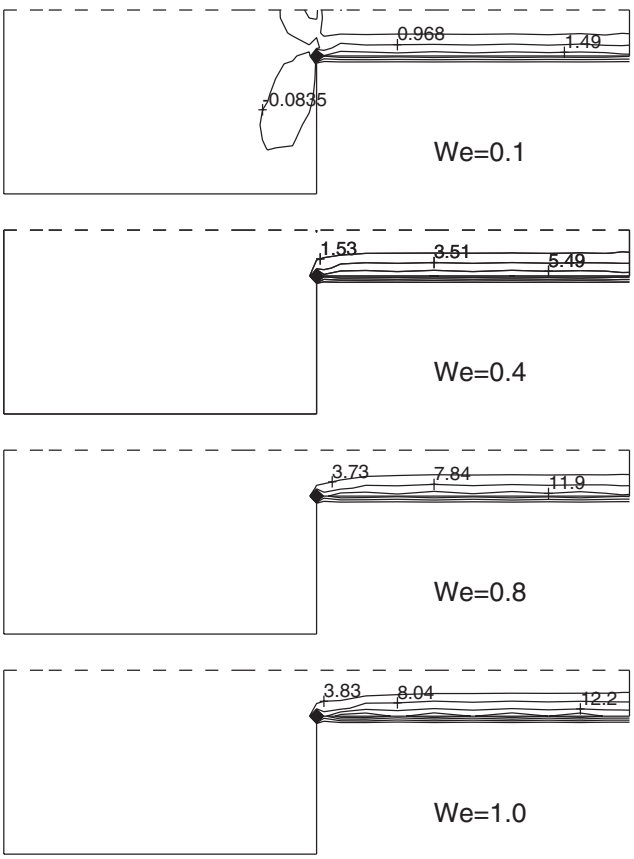

Figure 11. Comparison of contours for stress τ_{xx} with different We when $Re = 1.0$.

Figure 11 shows a comparison of stress component τ_{xx} with different Weissenberg numbers from $We = 0.1$ to 1.0. It is interesting to note that increasing the number of We results in almost the same pattern for the stress τ_{xx} contour profiles. It is clearly seen from these contours that the maximum values of τ_{xx} are always located at the re-entrant corner within the boundary layers and the minimum values are observed upstream of the re-entrant corner. As expected, the maximum values of τ_{xx} increase with increasing We. This can been seen more clearly in Figure 12, in which the stress τ_{xx} is plotted along the line of $y = -1$ with different Weissenberg numbers. It is found that for all numbers We the positions of the maximum values of the stress τ_{xx} are always located at the point $x = 0$, which is the position of the re-entrant corner. However, it should be noted that the magnitudes of the maximum values of stress τ_{xx} are significantly different. This is clearly shown in Figure 12, where the maximum value of τ_{xx} is 4.6493, when $We = 0.1$, but is over 54.2844, when $We = 1.0$. This indicates that the maximum value of the stress τ_{xx} is more sensitive to the change of the Weissenberg numbers.

Figure 13 shows the contour plots for the shear stress τ_{xy} with different Weissenberg numbers at $Re = 1.0$. Unlike the dramatic changes in the magnitude of the stress τ_{xx} in the

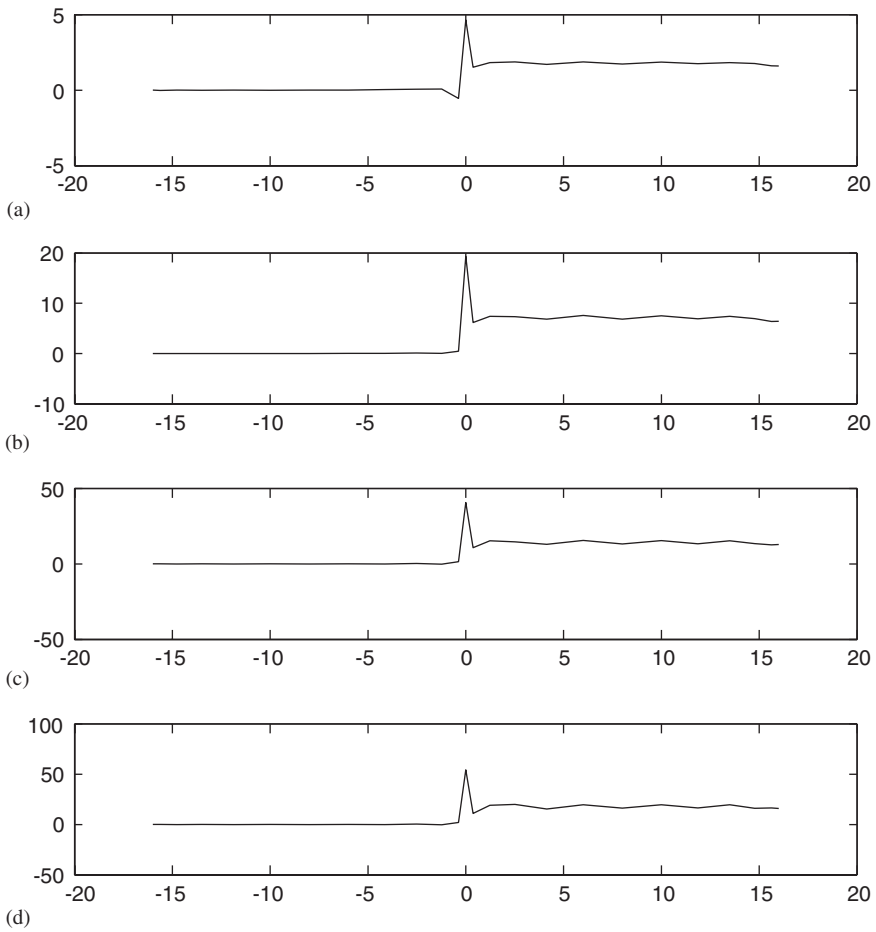

Figure 12. Comparison of the plots of τ_{xx} along the line $y=-1$ with different numbers of We, where (a) $We=0.1$, (b) $We=0.4$, (c) $We=0.8$ and (d) $We=1.0$ when $Re=1.0$. Note that the figures are plotted in different scales.

previous figure, we found that the values of the shear stress τ_{xy} are slightly different as We increases. However, it is seen that there exists a small hump from the re-entrant corner. Such a hump is enlarged with increasing We. It should be noted that this hump behaviour does not show in other components of the stress.

To further interrogate the differences in solutions for the stress components τ_{xy} and τ_{yy} for various Weissenberg numbers, we plotted these variables along the line $y=-1$ as shown in Figures 14 and 15 and found that all maximum values for both τ_{yy} and τ_{xy} are located at the re-entrant corner and are only slightly increased when We is increased. Actually, it is found that the maximum value of τ_{xy} for $We=0.1$ is 4.5457, and it increases only to 4.9119 when $We=1.0$. Similarly, the maximum value of τ_{yy} is 1.1530 for $We=0.1$, and is 1.5440 for $We=1.0$. It is worth pointing out that these solutions are corroborated by the results obtained in References [35].

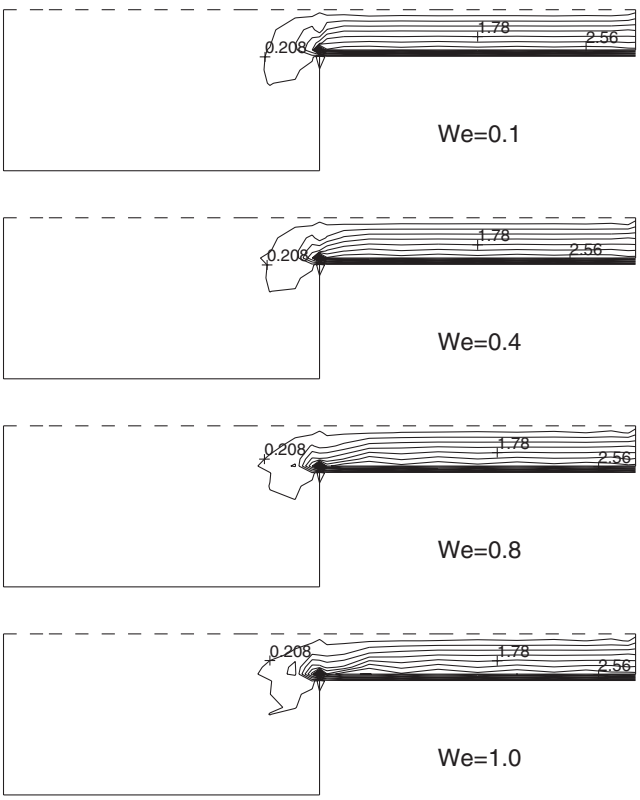

Figure 13. Comparison of contours for stress τ_{xy} with different We when $Re = 1.0$.

We now consider the vorticity effects resulting from different Weissenberg numbers. A comparison of the vorticity contours is illustrated in Figure 16, in which the Weissenberg numbers are $We = 0.1, 0.4, 0.8$ and 1.0, respectively, at $Re = 1.0$ on Mesh I. Although we found no significant difference in the pattern of these vorticity contours, there is a difference in locations of the rounded protuberance vorticity behind the re-entrant corner. This indicates that the vorticity has been slightly expanded when We increases. Such behaviour of vorticity has been reported in Reference [35] for high Weissenberg numbers.

Finally, we consider the numerical effects upon the EVSS scheme for the spectral element approximations. To do this, we therefore solve the benchmark problem described above by using both spectral element method with and without the EVSS schemes. Figure 17 shows the streamlines plotted with $We = 0.1, 0.4$ and 0.8, respectively, at $Re = 1.0$ for the solutions without using EVSS technique. Great insight can be obtained if Figure 17 is viewed along with Figure 9, where both figures show the comparisons of the streamlines plotted with different Weissenberg numbers. Comparing theses two figures, we found that the numerical solutions (streamlines) are almost identical with the small Weissenberg numbers for both methods, for instance, when $We = 0.1$ and 0.4. However, when the Weissenberg number is increased, it is found that the numerical solution with the EVSS scheme is more stable

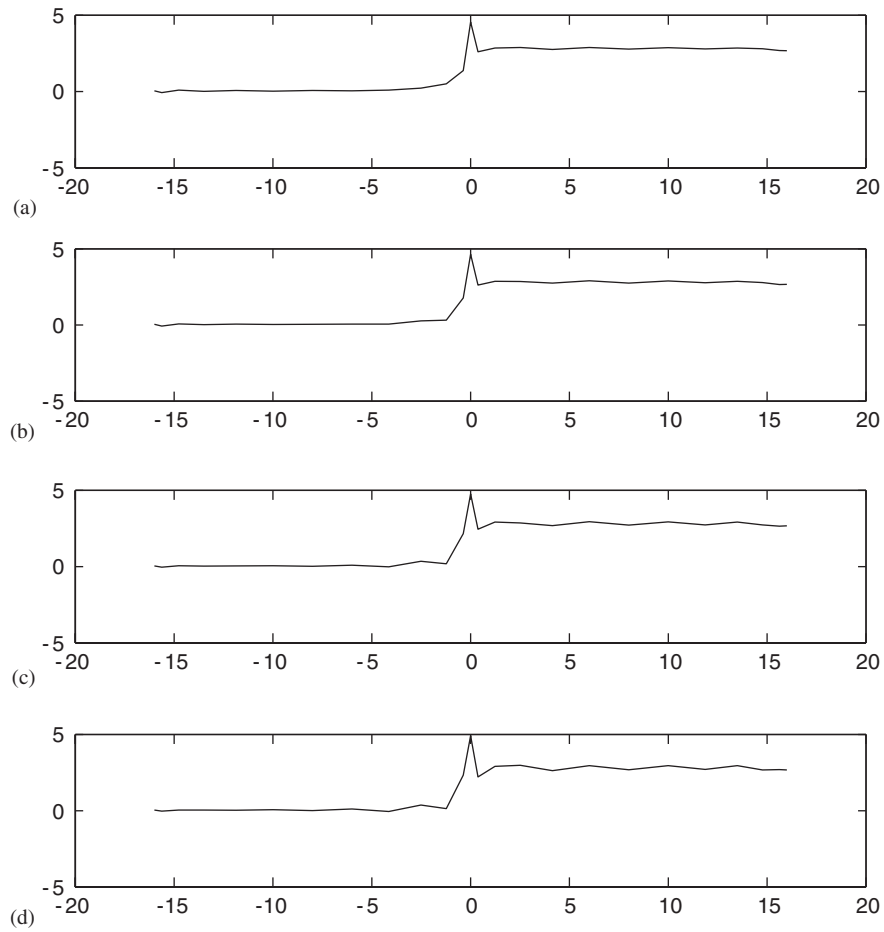

Figure 14. Comparison of the plots of τ_{xy} along the line $y=-1$ with different numbers of We, where (a) $We=0.1$, (b) $We=0.4$, (c) $We=0.8$ and (d) $We=1.0$ when $Re=1.0$.

than one without the EVSS. This is clearly shown in Figure 17, where some oscillations appeared on the streamlines near the re-entrant, when $We=0.8$. Such solutions become more and more oscillatory when We increases. In fact, we found that our numerical solutions without the EVSS procedure are divergent, when the Weissenberg number is over $We=0.8$. This phenomenon again demonstrates that the EVSS technique improves the numerical stability of the spectral element approximations in simulations of the contraction channel flows.

6. CONCLUSIONS

A spectral element method combined with the elastic viscous splitting stress method has been proposed to simulate an incompressible viscoelastic fluid in the planar contraction channel

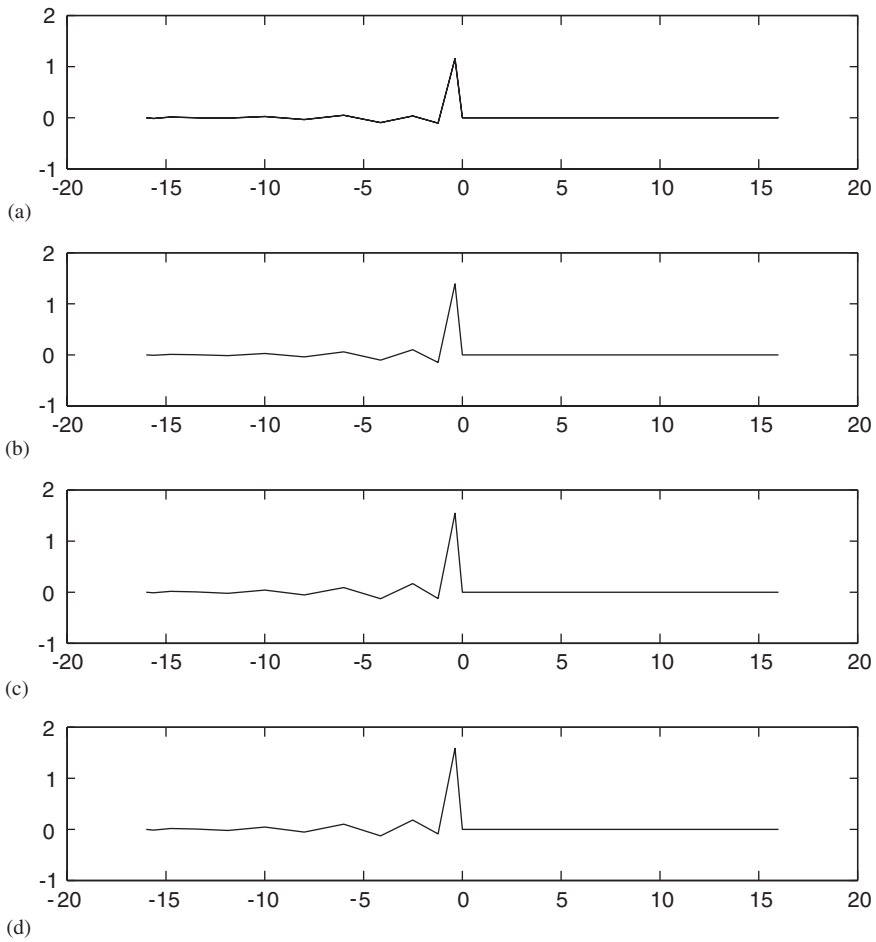

Figure 15. Comparison of the plots of τ_{yy} along the line $y=-1$ with different numbers of We, where (a) $We=0.1$, (b) $We=0.4$, (c) $We=0.8$ and (d) $We=1.0$ when $Re=1.0$.

flow. In this algorithm, a new variable, the rate of deformation tensor, has been introduced into the spectral element discretization formulations in order to enhance the stability and accuracy of the scheme. The pressure is obtained from the continuity and momentum equations based on the Uzawa iterative algorithm. The velocity, extra stress and the rate of deformation tensor are solved from the momentum and constitutive equations by the spectral element approximation with the EVSS procedure. Although in this paper the stress approximation space is chosen to be the same as the velocity space, and the rate of deformation approximation space is the same as the pressure space, it should be noted that a general guidance is still often lacking in what types of interpolations for the stress and the rate of deformation are still admissible.

In this paper, it has been shown that the spectral element method with the EVSS procedure is an effective practical approach for computing flows of an Oldroyd-B fluid. The numerical investigations have been applied to the planar four-to-one contraction channel flow problems

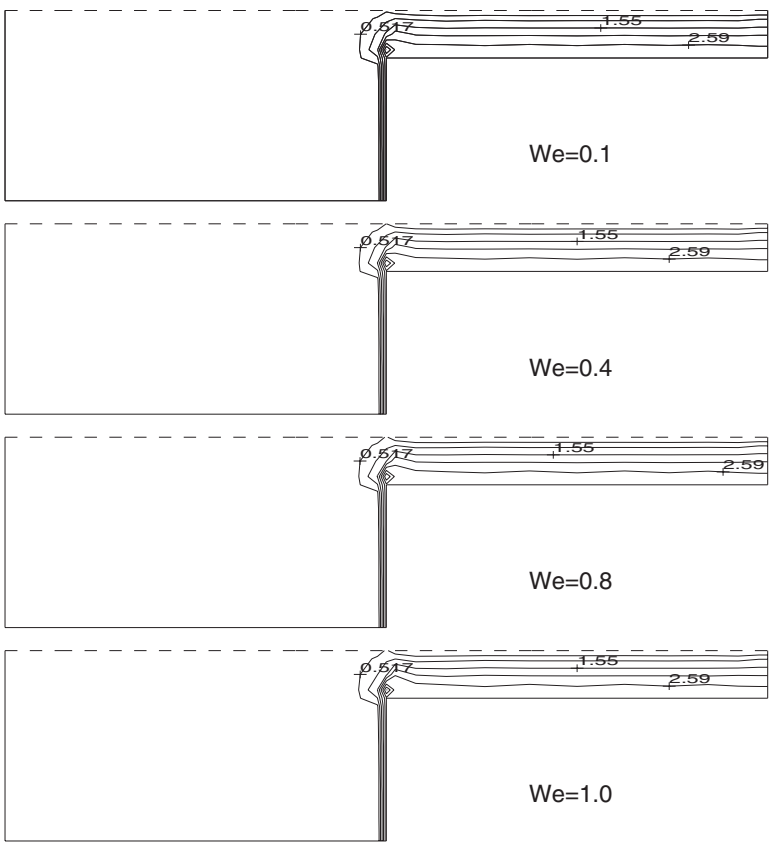

Figure 16. Comparison of vorticity contour plots with different We when $Re = 1.0$.

with various Weissenberg numbers. The simulation results indicated that, for an Oldroyd-B model, as the elasticity parameter We is increased the size of the corner vortex compares well with experimental measurements and other numerical predictions. The influence of the Weissenberg number We on the stress components is also discussed based on the numerical solutions. It is found that the maximum values of the stress are located at the re-entrant corner within the stress boundary layers. The values of τ_{xx} are dramatically increased as We increases, while the values of τ_{xy} and τ_{yy} are not sensitive to the change of We. Furthermore, the vorticity separation mechanism is also observed which grows with elasticity from the re-entrant corner. This observation is supported by the work of Sato *et al.* [35]. It should be noted that in all our calculations at a fixed level of inertia of $Re = 1.0$ and with increasing We, the spectral element approximation takes a very long time to reach a steady-state solution because of the time-dependent nature of the fluid motion and the instability of the extra stress started with an instantaneous increase of We. So the attempt to seek a higher upper limit on We has been stopped at the moderately value $We = 1.2$ for the present method, further work is needed to increase the limit of We.

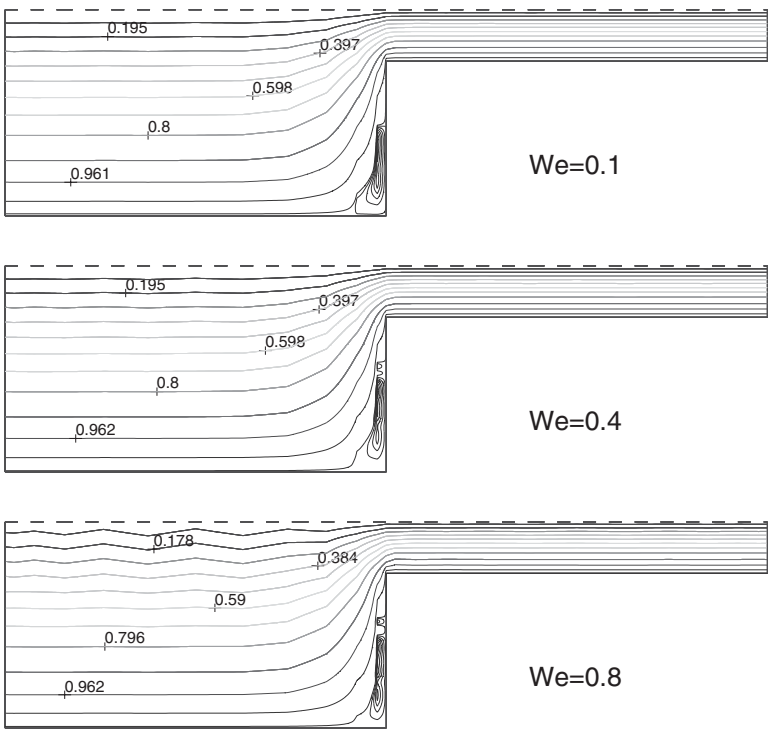

Figure 17. Streamlines for $We = 0.1$, $We = 0.4$ and $We = 0.8$, respectively, at $Re = 1.0$ without using EVSS scheme.

ACKNOWLEDGEMENTS

The authors are indebted for the many discussions with our colleagues within the Institute of Mathematical Simulation Sciences, De Montfort University (DMU). The computations were carried out at the School of Computing Sciences, DMU, whose excellent support is gratefully acknowledged. One of the authors (SM) has been financially supported by the research studentship from DMU.

REFERENCES

1. Barnes JF, Hutton JF, Walters K. *An Introduction to Rheology*. Elsevier: Amsterdam, 1989.
2. Bird R, Armstrong R, Hassager O. *Dynamics of Polymeric Liquids*, *Vol. I*: *Fluid Mechanics* (2nd edn.). Wiley: New York, 1987.
3. Crochet MJ, Davies AR, Walters K. *Numerical Simulation of non-Newtonian Flow*. Elsevier: Amsterdam, 1984.
4. Crochet M. Numerical simualtion of viscoelastic flow: a review. *Rubber Chemistry and Technology* 1989; **62**:426–455.
5. Fortin M, Pierre R. On the convergence of the mixed method of Crocher and Marchal for viscoelastic flows. *Computer Methods in Applied Mechanics and Engineering* 1989; **73**:341–350.
6. Fortin M, Fortin A. A new approach for the FEM simulation of viscoelastic flows. *Journal of Non-Newtonian Fluid Mechanics* 1989; **32**:295–310.
7. Marchal J, Crochet M. Hermitian finite elements for calculating viscoelastic flow. *Journal of Non-Newtonian Fluid Mechanics* 1986; **20**:187–207.
8. King R, Apelian M, Armstrong R, Brown R. Numerical stable finite element techniques for viscoelastic calculations in smooth and singular geometries. *Journal of Non-Newtonian Fluid Mechanics* 1988; **29**:147–216.

9. Chang P, Patten T, Finlayson B. Collocation and Galerkin finite-element methods for viscoelastic fluid flow I. Description of method and problem with fixed geometries. *Computers and Fluids* 1979; **7**:263–283.
10. Rajagopalan D, Armstrong R, Brown R. Finite element methods for calculation of steady, viscoelastic flow using constitutive equations with a Newtonian viscosity. *Journal of Non-Newtonian Fluid Mechanics* 1990; **36**:159–192.
11. van Schaftingen J, Crochet M. A comparison of mixed methods for solving the flow of a Maxwell fluid. *International Journal for Numerical Methods in Fluids* 1984; **4**:1065–1081.
12. Luo XL, Tanner RJ. A decoupled finite element streamline-upwind scheme for viscoelastic flow problems. *Journal of Non-Newtonian Fluid Mechanics* 1989; **31**:143–162.
13. Alves MA, Pinho AJ, Oliveira PJ. Effect of a high-resolution differencing scheme on finite-volume predictions of viscoelastic flows. *Journal of Non-Newtonian Fluid Mechanics* 2000; **93**:287–314.
14. Phillips TN, Williams AJ. Viscoelastic flow through a planar contraction using a semi-Lagrangian finite volume method. *Journal of Non-Newtonian Fluid Mechanics* 1999; **87**:215–246.
15. Phillips TN, Williams AJ. A semi-Lagrangian finite volume for Newtonian contraction flows. *SIAM Journal on Scientific Computing* 2001; **22**:2152–2177.
16. Aboubacar M, Webster MF. A cell-vertex finite volume/element method on triangles for abrupt contraction viscoelastic flows. *Journal of Non-Newtonian Fluid Mechanics* 2001; **98**:83–106.
17. Huilgol RR, Phan-Thien N. *Fluid Mechanics of Viscoelasticity*. Elsevier: Amsterdam, 1997.
18. Marchal J, Crochet M. A new mixed finite element for calculation viscoelastic flow. *Journal of Non-Newtonian Fluid Mechanics* 1987; **26**:77–115.
19. Guenette R, Fortin M. A new mixed finite-element method for computing viscoelastic flows. *Journal of Non-Newtonian Fluid Mechanics* 1995; **60**:27–52.
20. Baaijens FPT. Mixed finite-element methods for viscoelastic flow analysis: a review. *Journal of Non-Newtonian Fluid Mechanics* 1998; **79**:361–385.
21. Chauviere C, Owen RC. A new spectral element method for the reliable computation of viscoelastic flow. *Computer Methods in Applied Mechanics and Engineering* 2001; **190**:3999–4018.
22. Owen RG. *A posteriori* erro estimates for spectral element solutions to viscoelastic flow problems. *Computer Methods in Applied Mechanics and Engineering* 1998; **164**:375–395.
23. Li XK, Gwynllyw DRh, Davies AR, Phillips TN. On the influence of lubricant properties on the dynamics of two-dimensional journal bearings. *Journal of Non-Newtonian Fluid Mechanics* 2000; **93**:29–59.
24. Patera A. A spectral element method for fluid dynamics: laminar flow in a channel expansion. *Journal of Computational Physics* 1984; **54**:468–488.
25. Maday Y, Patera AT. Spectral element methods for the incompressible Navier–Stokes equations. In *State of the Art Surveys in Computational Mechanics*, Noor A, Oden J (eds), 1989; 71–143.
26. Brezza F. On the existence, uniqueness and approximation of saddle-point problems arising from Lagrange multiplies. *RAIRO Analyse Numerique* 1974; **8**:129–151.
27. Gerritsma M, Phillips T. Compatible spectral approximations for he velocity–pressure–stress formulation of the Stokes problem. *SIAM Journal of Computers* 1999; **20**:1530–1550.
28. Fletcher CJ. *Computational Techniques for Fluid Dynamics*. Springer: Berlin, Heidelberg, 1988.
29. Bristeau M, Glowinski R, Periaux J. Numerical methods for the Navier–Stokes equations application to the simulation of compressible and incompressible viscous flows. *Computer Physics Report* 1987; **6**:73.
30. Temam R. *Navier–Stokes equations. Theory and Numerical Analysis*. North-Holland: Amsterdam, 1977.
31. Lipscomb G, Keunings R, Denn M. Implications of boundary singularities in complex geometries. *Journal of Non-Newtonian Fluid Mechanics* 1987; **24**:85–96.
32. Walters K, Webster M. On dominating elastico-viscous response in some complex flows. *Philosophical Transactions on Royal Society of London Series A* 1982; **308**:199–218.
33. Matallah H, Townsend P, Webster M. Recovery and stress-splitting schemes for viscoelastic flows. *Journal of Non-Newtonian Fluid Mechanics* 1998; **75**:139–166.
34. Carew E, Townsend P, Webster M. A Taylor–Petrov–Galerkin algorithm for viscoelastic flow. *Journal of Non-Newtonian Fluid Mechanics* 1993; **50**:253.
35. Sato T, Richardson S. Explicit numerical simulation of time-dependent viscoelastic flow problem by a finite element/finite volume method. *Journal of Non-Newtonian Fluid Mechanics* 1994; **51**:249–275.

